A&A 599, A130 (2017)
DOI: 10.1051/0004-6361/201629646

Astronomy & Astrophysics

Swift heavy ion irradiation of interstellar dust analogues

Small carbonaceous species released by cosmic rays

E. Dartois[1,⋆], M. Chabot[2], T. Pino[3], K. Béroff[3], M. Godard[4], D. Severin[5], M. Bender[5], and C. Trautmann[5,6]

[1] Institut d'Astrophysique Spatiale (IAS), CNRS, Univ. Paris Sud, Université Paris-Saclay, 91405 Orsay, France
e-mail: emmanuel.dartois@ias.u-psud.fr
[2] Institut de Physique Nucléaire d'Orsay (IPNO), IN2P3-CNRS, Univ. Paris Sud, Université Paris-Saclay, 91405 Orsay, France
[3] Institut des Sciences Moléculaires d'Orsay (ISMO), CNRS, Univ. Paris Sud, Université Paris-Saclay, 91405 Orsay, France
[4] Centre de Sciences Nucléaires et de Sciences de la Matière (CSNSM), CNRS/IN2P3, Univ. Paris Sud, Université Paris-Saclay, 91405 Orsay, France
[5] GSI Helmholtzzentrum für Schwerionenforschung, 64291 Darmstadt, Germany
[6] Technische Universität Darmstadt, 64287 Darmstadt, Germany

Received 3 September 2016 / Accepted 21 December 2016

ABSTRACT

Context. Interstellar dust grain particles are immersed in vacuum ultraviolet (VUV) and cosmic ray radiation environments influencing their physicochemical composition. Owing to the energetic ionizing interactions, carbonaceous dust particles release fragments that have direct impact on the gas phase chemistry.
Aims. The exposure of carbonaceous dust analogues to cosmic rays is simulated in the laboratory by irradiating films of hydrogenated amorphous carbon interstellar analogues with energetic ions. New species formed and released into the gas phase are explored.
Methods. Thin carbonaceous interstellar dust analogues were irradiated with gold (950 MeV), xenon (630 MeV), and carbon (43 MeV) ions at the GSI UNILAC accelerator. The evolution of the dust analogues is monitored in situ as a function of fluence at 40, 100, and 300 K. Effects on the solid phase are studied by means of infrared spectroscopy complemented by simultaneously recording mass spectrometry of species released into the gas phase.
Results. Specific species produced and released under the ion beam are analyzed. Cross sections derived from ion-solid interaction processes are implemented in an astrophysical context.

Key words. astrochemistry – cosmic rays – dust, extinction – evolution – solid state: refractory – methods: laboratory: solid state

1. Introduction

Astronomical observations of the diffuse interstellar medium and dust components of molecular clouds set constraints on the composition of organic solids and large molecules in the Galaxy. The observed emission of dust grains and interstellar absorption spectra result from the superposition and mixing of many different galactic environments and dust grains components, allowing the interstellar dust life cycle to be monitored. Dust is produced in the surroundings of several stellar sources, supernovae, clouds; as it travels through the Galaxy, it is exposed to various radiation environments (UV, cosmic rays) that will modify its structure and/or composition. Among the carbonaceous dust candidates, hydrogenated amorphous carbons (a-C:H) and other materials with various aromatic/aliphatic mixed structures dominate. The destruction of carbonaceous dust particles and chemical modifications in VUV-exposed regions have led to the observation of variations of emission features in the infrared at interfaces of clouds (e.g., Pilleri et al. 2015). Small hydrocarbons were identified mainly through their rotational transitions (e.g., Fuente et al. 2003; Teyssier et al. 2004; Gerin et al. 2005; Pety et al. 2012; Guzmán et al. 2015). The vacuum ultraviolet (VUV) photolysis of a-C:H dust particles liberates molecules in the gas phase that help explain the anomalously high abundances of some hydrocarbon species observed in the gas phase in several astrophysical environments, such as in a photon-dominated interface (Alata et al. 2014, 2015).

In addition to the ultraviolet photon field, carbonaceous dust grains are also exposed to energetic ions from the cosmic-ray background. So far, the evolution of the chemical composition of interstellar dust analogues have mainly been followed by infrared spectroscopy, at low ion energies (e.g., Mennella et al. 2003) or higher energies at room temperature (e.g., Godard et al. 2011), giving insight into the timescale of chemical modifications and destruction.

In this project, we complement earlier laboratory experiments on interstellar analogues in order to better understand the influence of energetic ions on the compositional changes of dust grains and species released into the gas phase. The experiments were performed by irradiating different hydrogenated carbonaceous analogue samples with 40–950 MeV ions and analyzing beam induced effects by in situ infrared spectroscopy in combination with measurements of volatile components by means of quadrupole mass spectrometry.

2. Experiments

Hydrogenated interstellar amorphous carbon analogues films (a-C:H samples) were prepared at IAS (Orsay) by plasma-enhanced

⋆ Experiments performed at the GSI, Germany. Part of this work has been financed by the French INSU-CNRS program "Physique et Chimie du Milieu Interstellaire" (PCMI).

Table 1. Irradiations parameters and deduced a-C:H destruction cross sections.

Ion	Ion energy (MeV)	Fluence Max (cm^{-2})	S_e [a] (MeV mg^{-1} cm^{-2}) [eV/Å]	Projected range (μm)	a-C:H Thickness (μm)	T (K)	σ [b] (10^3 Å^2)	N_{CH}(a-C:H) [c] (10^{19} cm^{-2})	f [d]
$^{197}Au^{25+}$	945.4	8×10^{11}	126 [1500]	74.7	0.63 ± 0.16	300	9.15 ± 1.3	0.35 ± 0.09	0.53
$^{132}Xe^{21+}$	633.1	5×10^{12}	92 [1100]	64.5	2.2 ± 0.5	300	3.12 ± 0.1	1.23 ± 0.30	0.79
		2×10^{12}			3.3 ± 0.8	100	3.35 ± 0.3	1.82 ± 0.45	0.48
		2×10^{12}			3.7 ± 0.9	40	2.94 ± 0.2	2.07 ± 0.52	0.44
$^{12}C^{2+}$	43.2	2×10^{14}	3.6 [44]	66.4	7.3 ± 1.7	300	0.0245 ± 0.004	4.04 ± 0.97	0.37
		2×10^{14}			5.7 ± 1.4	25	0.0323 ± 0.011	3.16 ± 0.79	0.44
		1×10^{14}			4.7 ± 1.2	25	0.0321 ± 0.019	2.62 ± 0.65	0.27

Notes. [(a)] Electronic stopping power, calculated using the SRIM-2013 code (Ziegler et al. 2010), with an H/C of 1 and a density of 1.2g/cm^3 (as in Godard et al. 2011). [(b)] CH bonds destruction cross section determined by fitting an exponential function $\propto \exp(-\sigma \times \text{fluence})$ to the CH column density evolution with fluence shown in the insets of Figs. 1 and 4. [(c)] Column density of CH bonds locked in the CH_2 and CH_3 group of the a-C:H film. See Sect. 3.1 for details. [(d)] Fraction of initial N_{CH} modified upon irradiation.

chemical vapor deposition (PECVD), where radicals and ions resulting from a low-pressure radio-frequency (RF) plasma (at 2.45 GHZ) of CH_4 gas are deposited on a ZnSe substrate under vacuum. Details of this method are described in previous works (Godard et al. 2011, 2010; Alata et al. 2014, 2015). The typical deposition time required to produce a film several micrometers thick is fifteen minutes. After the film is produced, the chamber is filled with N_2 at a pressure slightly higher than atmosphere and the substrate is mounted on an aluminum holder (2014 campaign) or gold coated (2015 campaign) copper holder, placed in small stainless steel chambers, evacuated with a dry primary vacuum pump, and then transported to GSI under vacuum.

The irradiation experiments were performed at the M3-beam line of the UNILAC of GSI[1] Helmholtzzentrum für Schwerionenforschung (Darmstadt, Germany). During the different beam times, we used the following ions : $^{197}Au^{25+}$ (at 945.4 MeV, July 2014), $^{132}Xe^{21+}$ (at 633.1 MeV, September 2014), and $^{12}C^{2+}$ (at 43.2 MeV, September 2015). The electronic stopping powers of the different ions were calculated using SRIM (the Stopping and Range of Ions in Matter; Ziegler et al. 2010), with an H/C of 1 and a density of 1.2 g/cm^3 (as in Godard et al. 2011) and are summarized in the Col. 4 of Table 1. In all cases, the ions' depths of implantation (≈64−75 μm) are much larger than the thickness of the film (≤10 μm).

The base pressure of the irradiation chamber was a few 10^{-8} mbar. Most experiments were performed on an infrared transmitting substrate that was cryocooled to 25−40 K. To investigate the quality of the a-C:H samples and beam coupling, a test beam time with Au ions took place at room temperature only and at a pressure of about 1.3×10^{-7} mbar. The xenon beam was used to irradiate a-C:H analogues at different temperatures (300, 100, and 40 K). The carbon beam was used to irradiate a-C:H analogues at 300 K and down to about 25 K. The low temperature irradiations were immediately followed by a post-irradiation temperature programmed desorption (TPD, ~5 K/min) measurement in order to sublimate and monitor species formed and trapped in the irradiated film. During the irradiation and TPD, gas phase species were monitored by means of quadrupole mass spectrometry (MKS Microvision). Blank mass spectra were recorded at room temperature, during the cooling down period, and during a blank experiment, i.e., a full cryocooling +TPD cycle experiment without beam. This enabled us to record the level of contaminant signals (dominated by H_2O, N_2, and O_2) in the mass spectra. During the $^{12}C^{2+}$ irradiation campaign (September 2015), a calibrated leak and an absolute pressure gauge were installed on the irradiation chamber and used to calibrate the absolute gas flow of the experiment for H_2, CH_4, and C_2H_2, the main species released under irradiation. The M3 beam line houses a Nicolet FTIR spectrometer (Magna 550, spectral resolution 1 cm^{-1}) equipped with a MCT detector. This setup allowed us to record the infrared film transmittance (from 6000 to 650 cm^{-1}) in situ during beam stops at different fluence steps. The IR spectra are recorded under an angle of 45° from the a-C:H film normal. Infrared spectra were also recorded during the a-C:H TPD for films irradiated at 100, 40, and 25 K. For the gold irradiation test experiments, the IR spectral range covered only allowed monitoring of the stretching mode bands.

3. Results

3.1. Infrared measurements

The absorption spectra in the infrared region between 4250 and 600 cm^{-1}, as a function of irradiation fluence are presented in Figs. 1 and 4 for the a-C:H films during the irradiations with Xe ions (at 300, 100, and 40 K) and C ions (at 300 and 25 K). For the irradiation with Au ions, the IR spectra were only recorded in the range of the CH stretching mode (not shown).

The primary effect of the irradiation is an effective destruction of the C-H component. The optical depth of the bands of the methyl and methylene group (stretching modes around 2900 cm^{-1}, deformation modes around 1460 and 1380 cm^{-1}) decrease upon irradiation. The integrated optical depth of the stretching modes as a function of the fluence are shown in the insets of the figures. The column density of CH bonds locked in the CH_2 and CH_3 group of the a-C:H films is estimated from the stretching modes bands, and using the integrated absorption cross sections $A^{as}_{CH_3} = 1.25 \times 10^{-17}$ cm/CH_3 and $A^{as}_{CH_2} = 8.4 \times 10^{-18}$ cm/CH_2 (see Dartois et al. 2004, for details), divided by $\sqrt{2}$ to take into account the IR measurements performed at 45° of the thin film normal. The corresponding cross section σ of CH- bond destruction is determined by fitting an exponential function $\propto \exp(-\sigma \times \text{fluence})$ to the CH column density

[1] http://www.gsi.de

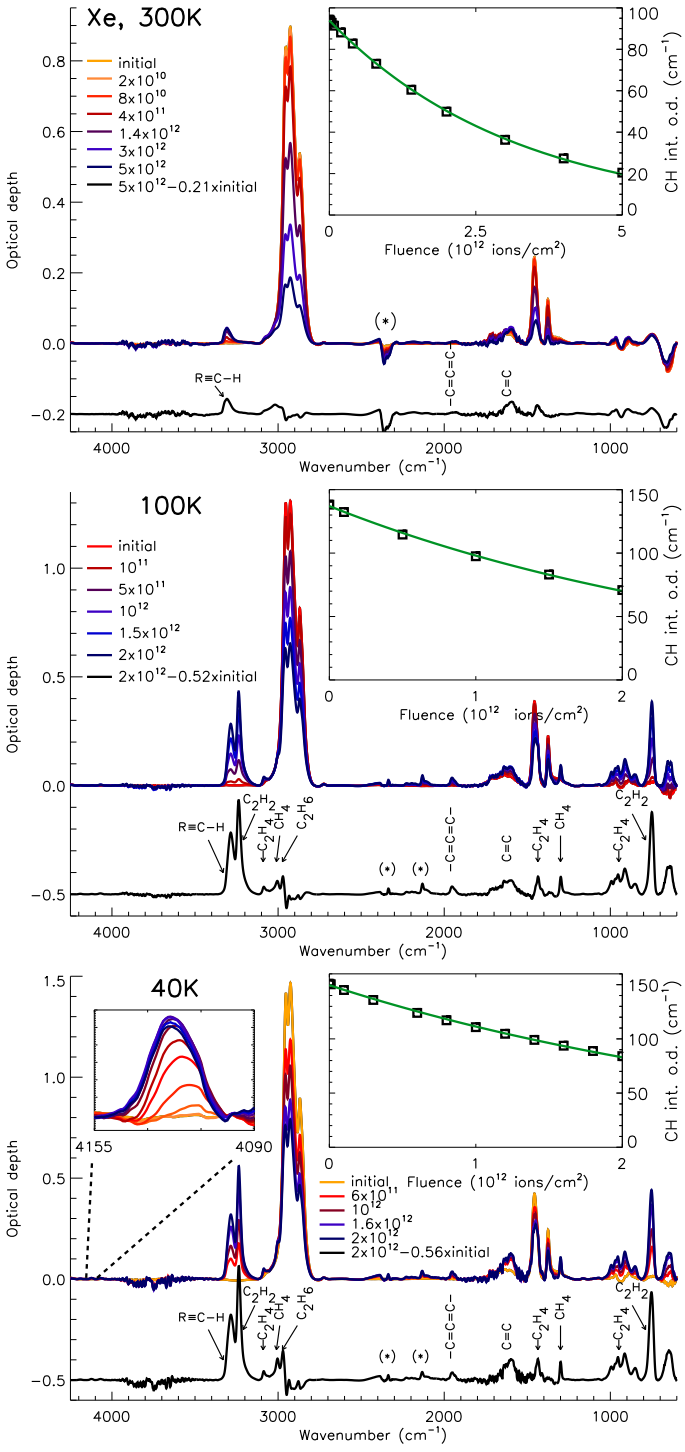

Fig. 1. Infrared optical depth spectra of the a-C:H sample, irradiated with $^{132}Xe^{21+}$ at 300 K (*upper panel*), 100 K (*center panel*), and 40 K (*lower panel*), as a function of fluence. The lower spectrum in each panel is the difference between the spectrum recorded at the highest fluence and the pristine material scaled to the CH stretching mode intensity to show the newly formed bonds in the material with a higher contrast. The upper right insets show the integrated optical depth for the CH bonds (squares) as a function of fluence. The lines are exponential fits that allow us to determine the destruction cross section (see text for details). At 40 K the inset shows the appearance of a band around 4120 cm^{-1} associated with H_2 formed and trapped in the bulk.

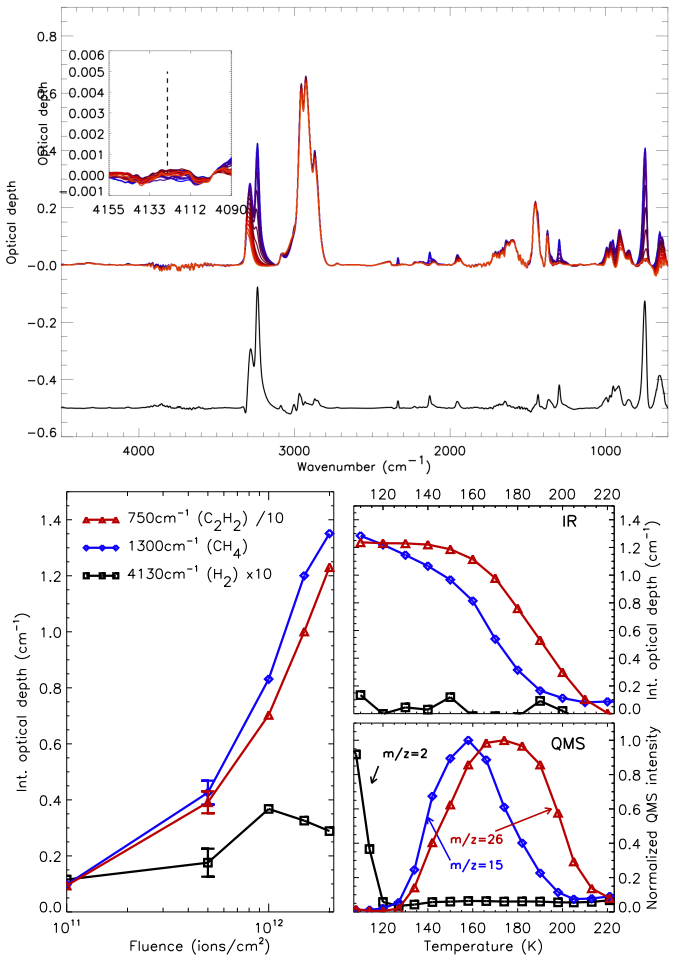

Fig. 2. *Upper panel*: infrared optical depth spectra of a-C:H sample during TPD, after irradiation to a fluence of 2×10^{12} ion/cm^2 with $^{132}Xe^{21+}$ at 100 K. The inset shows a close-up of the H_2 absorption region. *Lower panel* (*left*): integrated optical depth for H_2, CH_4, and C_2H_2 bands as a function of fluence. Evaluated errors bars on the integration are shown for one fluence; (*right*): evolution of infrared and mass signals of the considered molecules during TPD.

evolution with fluence, shown as solid curves in the figure insets. We note that we do not use the Maret et al. prescription as in Godard et al. (2011) since the fluence range is too low to constrain such a model. Our assumption corresponds to first-order kinetics. The cross sections deduced from our experiments are summarized in Table 1; they do not change significantly with the film temperature. In the 300 K experiments, new bands appear around 3300, 1950, and 1600 cm^{-1}, characteristic group frequencies for acetylenic ≡C-H, cumulenic C=C=C, and sp^2 C=C stretching modes, evidencing beam induced chemical changes.

Spectra of films irradiated with Xe ions (100 and 40 K) and with C ions (25 K) display additional bands of species produced and trapped in the a-C:H network species, corresponding to C_2H_2 (at about 3240 and 770 cm^{-1}), CH_4 (at about 3010 and 1300 cm^{-1}), C_2H_4 (at about 950 cm^{-1}), and C_2H_6 (at about 2975 cm^{-1}). Acetylene and methane absorption bands are rather well isolated from other absorption bands. At the lowest temperature, a weak absorption band around 4125 cm^{-1} is attributed to H_2 produced and retained inside the a-C:H film (close-ups are shown in the insets of Figs. 1–4). In Figs. 2, 3, and 5, the IR spectra recorded during TPDs are shown in the upper panel. The monitoring of the H_2, CH_4, and C_2H_2 molecules via IR spectroscopy and mass spectrometry (MS), at specific chosen fragmentation pattern masses attributed to these species, are

Table 2. Analysis of low-temperature infrared spectra for selected spectrally isolated vibrational modes.

Species	Band position (cm^{-1})	A^a (cm/molecule)	$^{132}Xe^{21+}$ (100 K) $\int \tau d\nu^b$ (cm^{-1})	$^{132}Xe^{21+}$ (100 K) N^c (10^{16} cm^{-2})	$^{132}Xe^{21+}$ (40 K) $\int \tau d\nu^b$ (cm^{-1})	$^{132}Xe^{21+}$ (40 K) N^c (10^{16} cm^{-2})	$^{12}C^{2+}$ (25 K) $\int \tau d\nu^b$ (cm^{-1})	$^{12}C^{2+}$ (25 K) N^c (10^{16} cm^{-2})
H_2	4130	$<9.4 \times 10^{-20}$	$<2.9 \times 10^{-2}$	–	0.125	>94	0.272	>205
CH_4	1300	$8.0 \pm 1.5 \times 10^{-18}$	1.35	11.9 ± 2.2	1.47	13.0 ± 2.4	0.35	3.06 ± 0.57
C_2H_2	3240	$2.52 \pm 0.90 \times 10^{-17}$	14.6	40.9 ± 14.6	17.3	48.5 ± 17.3	0.59	1.68 ± 0.60
C_2H_2	760	$2.11 \pm 0.27 \times 10^{-17}$	12.3	41.2 ± 5.3	14.6	48.9 ± 6.3	0.61	2.04 ± 0.26

Notes. [a] See text for details on the integrated absorption cross sections A used to derive the column densities; [b] Integrated optical depth over the band. [c] Column density for the considered species.

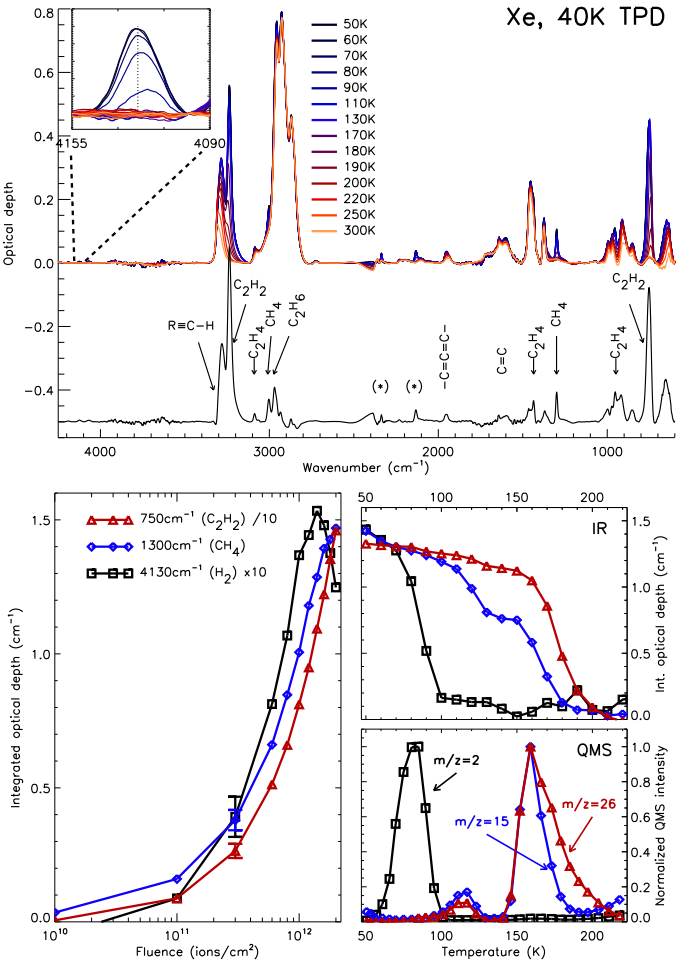

Fig. 3. Same information as shown in Fig. 2 but for irradiation at 40 K.

presented in the lower panels. The attribution of the IR bands to these species is corroborated by the evolution during irradiation but more strongly by the correlated decrease in their IR bands observed during TPD and the increase in the masses recorded when the species diffuse and sublimate. The temperature where maximum desorption is observed with MS lies in the 80−140 K range for H_2 (depending on film thickness) and about 160−250 K and 180−250 K for CH_4 and C_2H_2, respectively. The maximum temperatures shifts toward higher temperature for thicker films occur because the molecules diffuse in the bulk of the film. In the 100 K experiment, most of the H_2 molecules had time to diffuse out during the irradiation time.

The column densities for these species at the highest fluence are evaluated and reported in Table 2. The integrated absorption cross section A for H_2 was taken from the literature for H_2 embedded in an ice mixture: $A_{H2}^{4130\ cm^{-1}} = 9.4 \pm 0.4 \times 10^{-20}$ cm/molecule (Sandford & Allamandola 1993). The activity of the H_2 mode, when embedded in a-C:H is unknown. We assume that the corresponding A would be higher in a polar ice mixture than in a-C:H. The integrated absorption cross sections used to derive the column densities for the other species are $A_{CH4}^{1300\ cm^{-1}} = 8.0 \pm 1.5 \times 10^{-18}$ cm/molecule (mean from Boogert et al. 1997; Kerkhof et al. 1999; Herrero et al. 2010; Gerakines & Hudson 2015), $A_{C2H2}^{3240\ cm^{-1}} = 2.52 \pm 0.90 \times 10^{-17}$ cm/molecule, and $A_{C2H2}^{768\ cm^{-1}} = 2.11 \pm 0.27 \times 10^{-17}$ cm/molecule (mean from Hudson et al. 2014; Knez et al. 2012; Khanna et al. 1988; Boudin et al. 1998). A $\sqrt{2}$ correction factor has been applied to obtain normal column densities, taking into account that the IR measurements were performed under 45° with respect to the film surface. For H_2, the column density produced is higher than measured in the IR, as a fraction may have escaped by diffusion/sublimation during the irradiation.

The abundance ratio of the main species condensed is compatible with the one measured by MS during the TPD and discussed in the next section. Although spectroscopically well identified in these experiments, the column density of H_2 cannot be determined at a higher precision than an order of magnitude in the IR using previous estimates of the band strength for H_2 in ice. In fact, the induced IR activity and band strength of the transition for H_2 trapped in an a-C:H film is different (see Sect. 3.4).

3.2. Mass measurements

The time-integrated QMS spectra, recorded during the irradiations of a-C:H with $^{197}Au^{21+}$, $^{132}Xe^{21+}$, and $^{12}C^{2+}$ at room temperature (~300 K) are shown in Fig. 6 and in the upper panels of Figs. 7 and 8. These spectra were background subtracted to eliminate the contributions from the residual vacuum gases (H_2O, N_2, O_2, etc.). However, the masses where these residuals may still contribute are indicated in the figures. For the low-temperature irradiations, the species produced in the bulk slowly diffuse in the film, and are mainly released during TPD. This is evidenced by comparing the TPDs integrated signals in the middle and lower panels of Figs. 7 and 8 to the signal at 300 K, scaled to the same fluence, except for H_2, which diffuses out rapidly even at 100 K (see details below).

The species contributing to the mass spectra are retrieved by a matrix analysis, using a fragmentation pattern matrix **M** for the

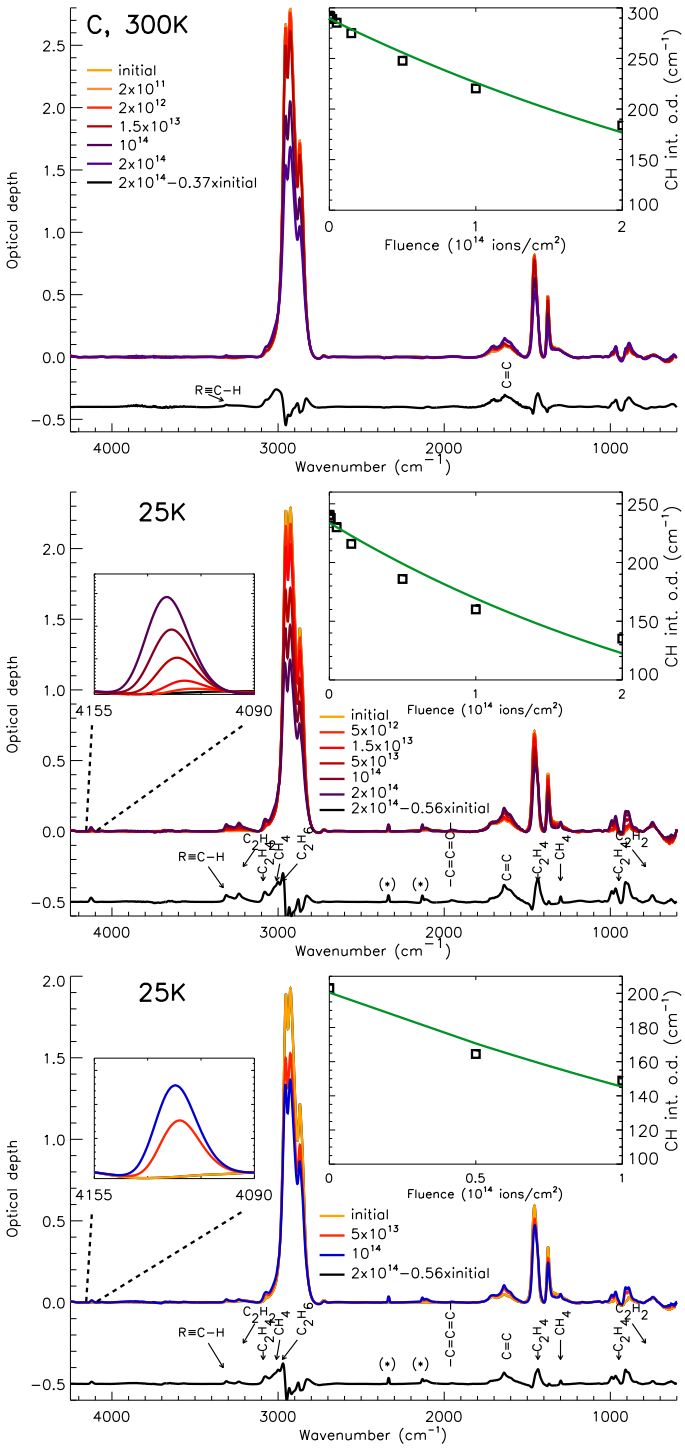

Fig. 4. Same as Fig. 1 for a-C:H sample irradiated with $^{12}C^{2+}$ ions at 300 K (*upper panel*) and 25 K for two independent experiments (*middle and lower panels*) as a function of fluence. At 25 K the insets show the appearance of a band around 4120 cm^{-1} associated with H_2 formed and trapped in the bulk.

species. The linear least-squares equation

$$\min_x \|w_i(\mathbf{M}\,\boldsymbol{x} - \mathrm{s})\|_2^2 \qquad (1)$$

is minimized, and yields the contribution of a specific species. In this equation, s is the vector of QMS measured intensities at the different masses-over-charge (m/z) channels, x denotes the species contributions that have to be divided by the ionization cross sections to retrieve their relative contributions, and

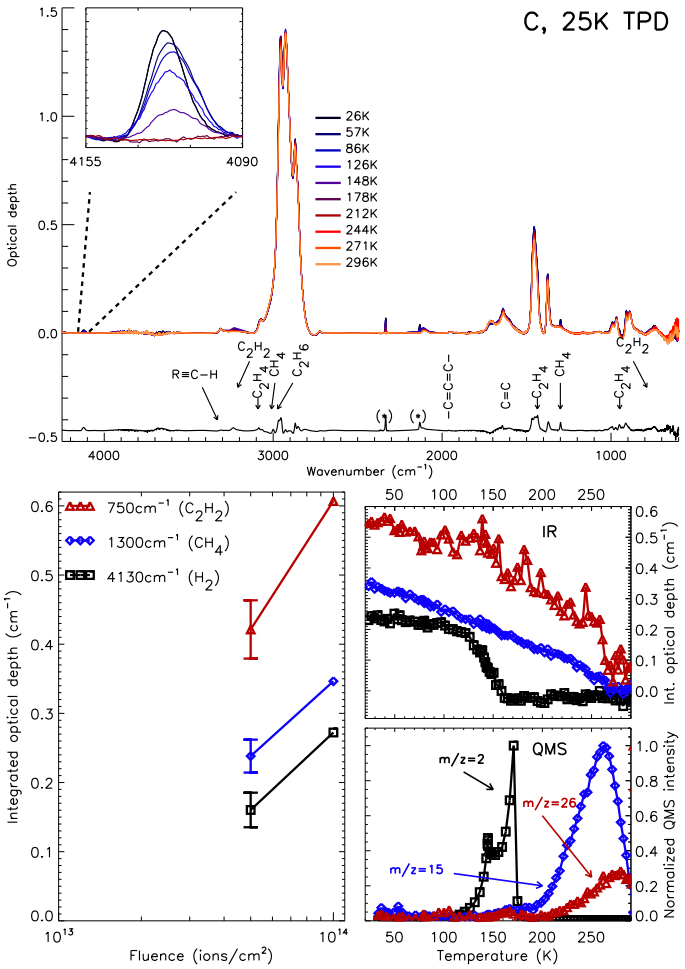

Fig. 5. Same as Fig. 3 for a-C:H sample during TPD after irradiation to a fluence of 1×10^{14} ion/cm^2 with $^{12}C^{2+}$ ions at 25 K.

w_i is a weighting factor (equal to 1 or 0) to include only the measured m/z where the cracking patterns of the considered species contribute significantly or are known with sufficient accuracy. The matrix formed contains the fragmentation patterns for H_2, CH_4, C_2H_2, C_2H_4, C_2H_6, C_3H_4, C_3H_6, C_3H_8, C_4H_2, C_4H_4, C_4H_6, C_4H_8, C_4H_{10}, and the main contaminant residual gas species (H_2O, N_2, CO_2, CO, O_2). The fragmentation patterns and ionization cross sections for the electron impact ionization at 70 eV, corresponding to the QMS ionization source, are taken from the literature (Ward et al. 2011; King & Price 2007; Straub et al. 1998, 1997, 1996a,b) and the NIST database (www.nist.gov). For CH_4 and C_2H_2, the fragmentation pattern was directly evaluated from the QMS calibration presented in Sect. 3.3. The synthetic mass spectra resulting from these minimizations are shown by the blue histograms in Figs. 6–8, superimposed on the measured QMS spectra. The corresponding abundances derived, relative to CH_4, are given in Tables 3–5, respectively. The QMS spectra show the buildup of series separated by 12 m/z, associated with the number of carbon atoms implied in the species fragmenting. The relative abundances for a given C_xH_y are shown by C series in the tables.

We note that the produced high molecular weight species compared to the H_2 fraction increases with the stopping power of the ions. The CH_4/H_2 fraction measured with the C beam is similar to the yields measured for VUV photolysis (e.g., Alata et al. 2014), whereas for Xe and Au the $\sum_{i,j} C_iH_j/H_2$ rises significantly.

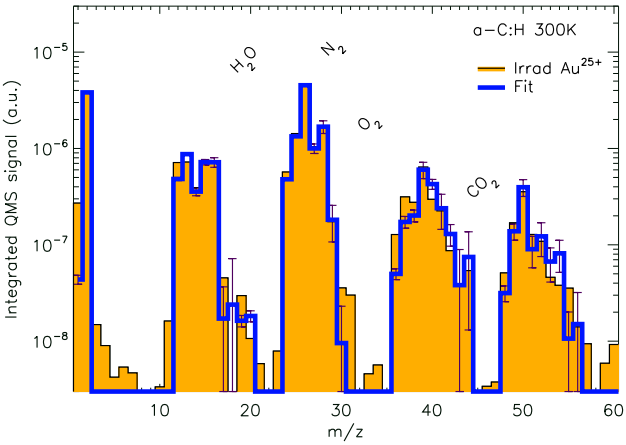

Fig. 6. QMS integrated signal for a-C:H sample irradiated with $^{197}Au^{25+}$ at 300 K (orange bars). The best model fit is shown in blue. The labels above mark the positions where residual contaminant gases could contribute.

Table 3. Abundance of species retrieved from QMS data for $^{197}Au^{25+}$ irradiations, normalized to CH_4 ($\pm 2\sigma$)

	Abundance
Species	300 K
H_2	$7.94 \pm {}^{3.17}_{0.79}$
CH_4	1.00 ± 0.103
C_2H_2	3.33 ± 0.083
C_2H_4 } C_2H_y	1.12 ± 0.077
C_2H_6	0.014 ± 0.066
C_3H_4	0.303 ± 0.057
C_3H_6 } C_3H_y	0.159 ± 0.063
C_3H_8	0.118 ± 0.064
C_4H_2	0.136 ± 0.041
C_4H_4	0.057 ± 0.044
C_4H_6 } C_4H_y	0.077 ± 0.055
C_4H_8	0.020 ± 0.048
C_4H_{10}	<0.047

3.3. QMS calibration

The principle of the QMS calibration was to inject gas into the chamber at a known flow rate and to relate it in an absolute way to the measured QMS signals. The gas flow was regulated by a MKS mass flow controller, calibrated in an absolute way by comparison to another gas injection system, namely injection through a small conductance calibrated capillary. This capillary (length 35 mm, diameter 1 mm) was previously used for absolute cross section measurements as described in Wohrer et al. (2000). The input pressure at the entrance of the capillary was measured with a Baratron capacitance manometer in the 10^{-2}–10^{-1} mbar range. With this system, flow rates Q as low as a few 10^{-3} sccm (standard cm^3 per minute) were injected. The residual pressure in the chamber was measured with an absolute Bayard-Alpert gauge. The calibrated flow rate measurement allowed us to deduce the pumping speed V_P in the chamber. The particle flow rate dN/dt is related to the residual pressure P_{res} and pumping

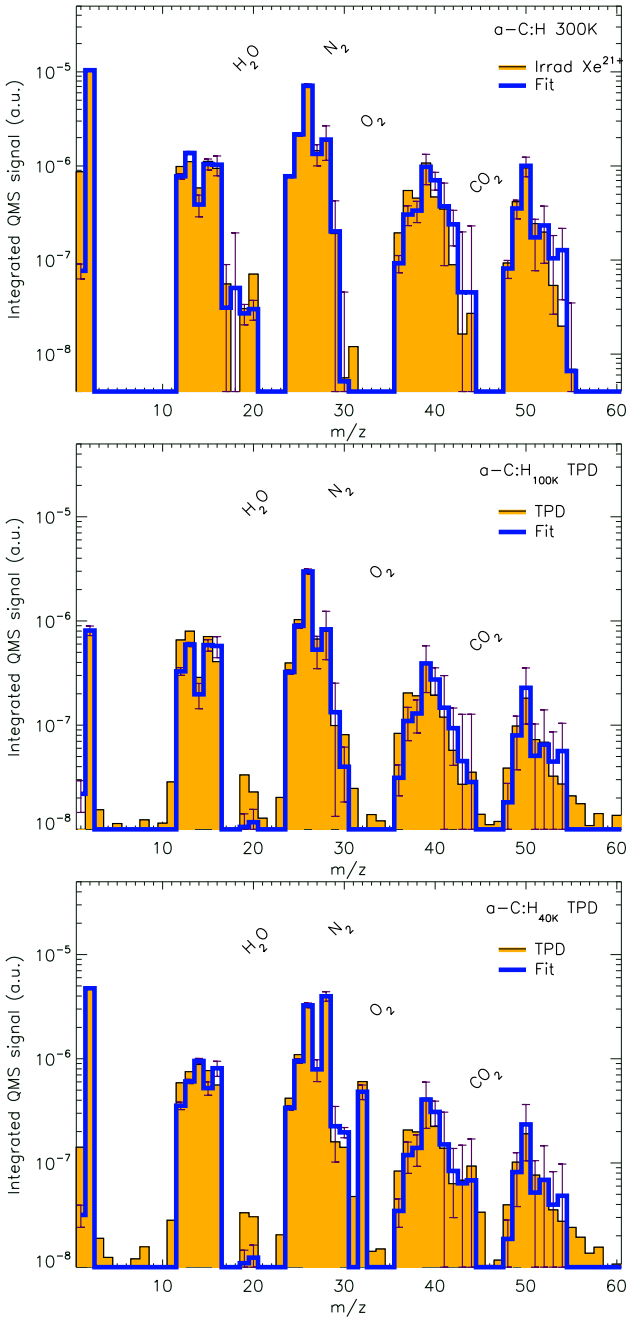

Fig. 7. QMS integrated signal for a-C:H sample irradiated with $^{132}Xe^{21+}$ (orange bars) at 300 K (*upper panel*), during the TPD after 100 K irradiation (*center panel*) and after 40 K irradiation (*lower panel*). The best model fits are shown in blue. The labels above mark the positions where residual contaminant gases could contribute.

speed V_P in the chamber by

$$\frac{dN}{dt} = 4.42 \times 10^{17} \times Q(\text{sccm}) = 4.42 \times 10^{17} \times a(T) \times P_{res}(\text{Torr}) \times V_P(\text{l/s}), \quad (2)$$

where $a(T) = 273/(T(K) \times 0.0127)$ is a temperature dependent coefficient relating Q(sccm) and Q(Torr.l/s) (Roth 1990; Wohrer et al. 2000). Equation (2) expresses the equilibrium reached between gas input (injection) and gas output (pumping). It allows dN/dt to be deduced by two different means, either directly through the flow rate Q or via the P_{res} plus V_P.

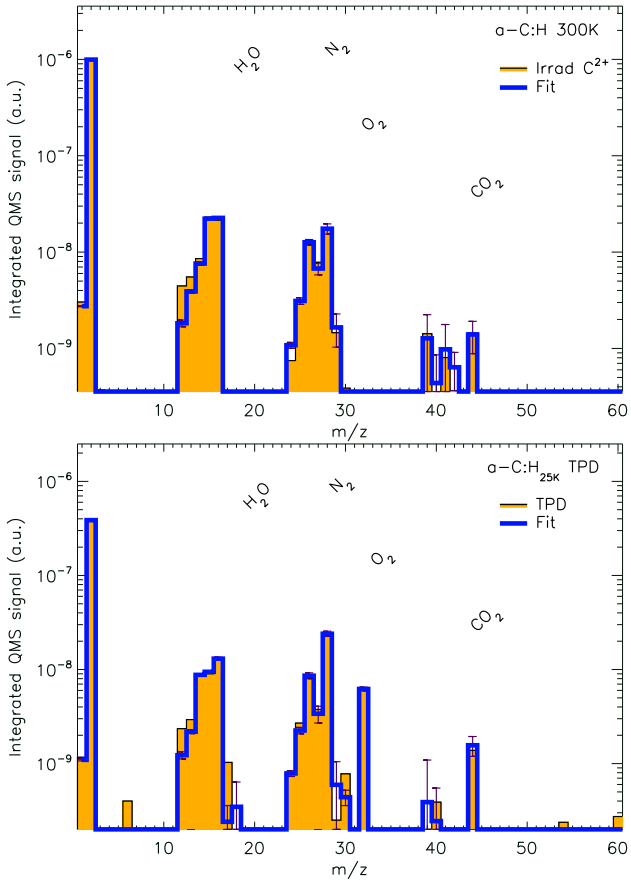

Fig. 8. QMS integrated signal for a-C:H sample irradiated with $^{12}C^{2+}$ (orange bars) at 300 K (*upper panel*), and during the TPD after 25 K irradiation (*lower panel*). The best model fits are shown in blue. The labels above mark the positions where residual contaminant gases could contribute.

Table 4. Abundance of species retrieved from QMS data for $^{132}Xe^{21+}$ irradiations and post irradiation TPD, normalized to CH_4 ($\pm 2\sigma$).

		Abundance		
Species		300 K	100 K TPD	40 K TPD
H_2		$15.00 \pm {}^{4.00}_{1.50}$	$2.06 \pm {}^{0.82}_{0.21}$	$14.45 \pm {}^{5.78}_{1.45}$
CH_4		1.00 ± 0.21	1.00 ± 0.20	1.00 ± 0.25
C_2H_2	C_2H_y	3.73 ± 0.17	2.84 ± 0.17	3.44 ± 0.20
C_2H_4	C_2H_y	1.00 ± 0.16	0.58 ± 0.15	0.88 ± 0.19
C_2H_6	C_2H_y	0.00 ± 0.13	0.13 ± 0.13	0.78 ± 0.16
C_3H_4	C_3H_y	0.343 ± 0.119	0.239 ± 0.114	0.331 ± 0.139
C_3H_6	C_3H_y	0.208 ± 0.131	0.139 ± 0.125	0.145 ± 0.152
C_3H_8	C_3H_y	0.091 ± 0.132	0.079 ± 0.126	0.000 ± 0.153
C_4H_2	C_4H_y	0.254 ± 0.085	0.097 ± 0.081	0.118 ± 0.098
C_4H_4	C_4H_y	0.077 ± 0.091	0.037 ± 0.087	0.047 ± 0.106
C_4H_6	C_4H_y	0.083 ± 0.113	0.066 ± 0.108	0.066 ± 0.131
C_4H_8	C_4H_y	0.002 ± 0.098	0.000 ± 0.094	0.014 ± 0.114
C_4H_{10}	C_4H_y	0.000 ± 0.096	0.017 ± 0.092	0.050 ± 0.112

Both methods gave similar results. It is worth mentioning that the pumping speed was found to be similar at room temperature (RT) and low temperature (LT) for the H_2 gas but not for CH_4, which shows a difference of a factor of about four. This difference was explained by the fact that CH_4 molecules stick on the cold substrate while light H_2 molecules do not. Calibration between dN/dt and the QMS signal IQMS (given as a pressure signal by the instrument) was done for various flow rates at RT and LT configurations (25 K). The number of particles N emitted under irradiation was then deduced by integrating Eq. (2) over time, i.e., by integrating IQMS over time (a quantity called integrated QMS signal in Figs. 1−3). Owing to an insufficient number of measurements (in particular for H_2) relatively large error bars for N values were reached, typically on the order of 30−50% (see below).

Table 5. Abundance of species retrieved from QMS data for $^{12}C^{2+}$ irradiations, normalized to CH_4 ($\pm 2\sigma$).

		Abundance	
Species		300 K	25 K TPD
H_2		$65.76 \pm {}^{26.3}_{6.58}$	$60.22 \pm {}^{24.1}_{6.02}$
CH_4		1.00 ± 0.03	1.00 ± 0.05
C_2H_2	C_2H_y	0.211 ± 0.022	0.385 ± 0.038
C_2H_4	C_2H_y	0.271 ± 0.021	0.302 ± 0.035
C_2H_6	C_2H_y	0.040 ± 0.018	0.089 ± 0.030
C_3H_4	C_3H_y	<0.015	<0.025
C_3H_6	C_3H_y	0.023 ± 0.017	<0.027
C_3H_8	C_3H_y	0.017 ± 0.017	<0.027

In the case of the a-C:H sample irradiated at RT by C ions up to a final fluence of 2×10^{14} ions/cm^2, we found that the number of emitted H_2 molecules deduced from the calibration was $N(H_2) = 1.12 \times 10^{19}$ (±50%). On the other hand, the number of destroyed CH_2 and CH_3 bonds deduced from IR absorption data (see Table 1) is $N(CH) = 4.04 \times 10^{19} \times 0.37$ cm^{-2} including the angle correction factor of $1/\sqrt{2}$ to take into account that the IR spectra were recorded under 45° with respect to the film surface. Taking into account the overall irradiated sample surface (2.4 cm^2), $N(CH) \approx 3.59 \times 10^{19}$ (±25%). Within the experimental uncertainties this value is compatible with two times N(H_2), i.e., the total number of released H atoms, as determined with the calibration. This proves that the H_2 formed in the sample due to broken CH_2 and CH_3 bonds is released in the gas phase. In the case of the a-C:H sample irradiated at LT by C^{2+} ions, the measurement of the number of emitted H_2 molecules extracted from the calibration coupled to the IR band for the H_2 molecules formed and trapped in the sample allows us to derive an oscillator strength for this band at low temperature, as explained below.

3.4. H_2 infrared band

The measurement of the IR band absorbance for the H_2 molecules formed and trapped in the a-C:H upon irradiation coupled to the H_2 gas phase QMS TPD signal, after QMS calibration, allows us to estimate an oscillator strength, in particular from the C irradiations at low temperature. In this experiment, H_2 is the main radiolytic product and the bulk of the H_2 produced by irradiation remains trapped in the a-C:H film at 25 K. Neglecting the very surface H_2 losses at 25 K, the integrated absorption cross section for the band observed around 4130 cm^{-1} is $A_{H2}^{4130\ \mathrm{cm}^{-1}} = \int \tau \mathrm{d}\nu / N_{H2}$, where the integral is taken over the measured IR absorption band, and N_{H2} is the total H_2 column density. The value of N_{H2} can be estimated from the N_{CH} column density decrease upon irradiation given in Table 1, $N_{H2}^{\mathrm{produced}} \approx \frac{1}{2} \times \eta \times N_{CH} \times f \approx \eta \times 3.54 \pm 0.88 \times 10^{18}$ cm^{-2}, where f and η correspond to the fraction of initial N_{CH} modified upon irradiation and the fraction of these H atoms released locked in the H_2 products, respectively. Looking at the QMS results

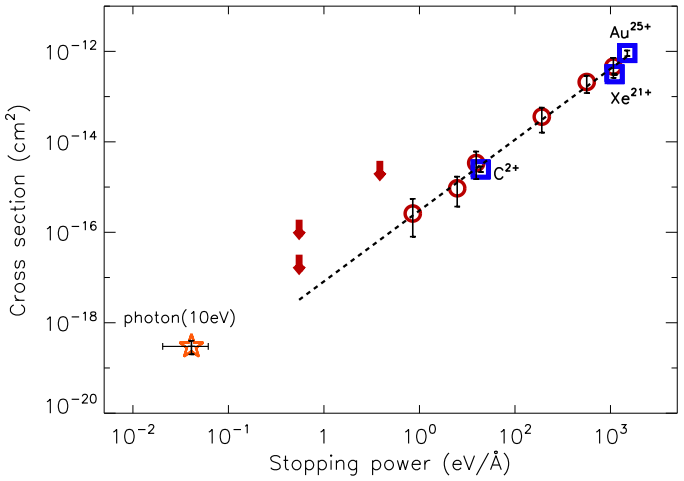

Fig. 9. CH destruction cross section as a function of stopping power: blue squares (this work), red circles and upper limit arrows (Godard et al. 2011). The equivalent cross section for ~10 eV photons are shown as orange stars. See text for details.

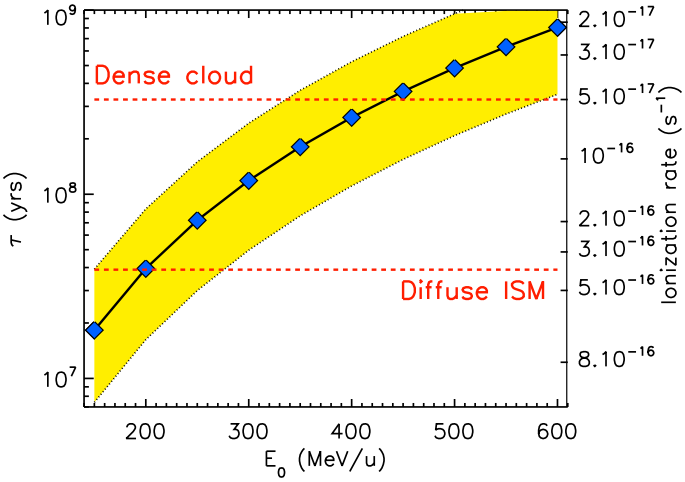

Fig. 10. CH destruction timescale associated with GCR irradiation as a function of the assumption on the low-energy flux contribution with the E_0 parameter. The colored area gives the error bar obtained from the reported uncertainties on the cross section. The corresponding ionization rate calculated is reported on the opposite axis. The observed ionization rates (Fig. 19 in Indriolo & McCall 2012) for dense (N_H column density $\approx 10^{23}$ cm^{-2}) and mean values for diffuse clouds are shown with dashed lines.

of Table 5, $\eta \approx 0.95$. It therefore follows that $A_{H2}^{4130\ cm^{-1}} \approx 5.72 \pm 1.42 \times 10^{-20}$ cm/molecule, to be compared to the value mentioned above, measured in an ice mixture: $A_{H2}^{4130\ cm^{-1}} = 9.4 \pm 0.4 \times 10^{-20}$ cm/molecule (Sandford & Allamandola 1993).

4. Astrophysical implications

4.1. Destruction timescale

The cosmic ray experimental simulations performed here extend previous studies at lower ion energies (Mennella et al. 2003; Godard et al. 2011), giving insight into the astrophysical implications for the evolution of interstellar a-C:H subjected to cosmic rays, and providing information on potential species to be released.

The CH destruction cross section dependence on the stopping power is analyzed by adding the Godard et al. (2011, Table C.1, a-C:H 1) cross sections, displayed in Fig. 9 to our measured cross sections (Table 1). The results of our experiments correspond to a bulk response, therefore considering the larger particles in a interstellar dust particles distribution. An order of magnitude for the corresponding valid size range can be estimated from the CH destruction cross section. For the measurements displayed in Fig. 9, the cross sections correspond to a projected radius of about 5–6 nm for the higher energy range investigated here (Xe, Au) and down to a few Å for C. We speculate that the destruction cross section might be higher if the particles are smaller, as the electronic relaxation can no longer proceed within the immediate surrounding of the a-CH network outside the core of the interaction.

For comparison, we also provide the equivalent cross section for 10 eV photons, assuming that the photon penetration depth is about where the optical depth of a-C:H film equals 1. This was estimated from the imaginary part of the refractive index (k) measured for the same analogues in the VUV (Gavilan et al. 2016), using the CH photolysis cross section of $\sigma \approx 3 \pm 0.9 \times 10^{-19}$ cm^2 from Alata et al. (2014) for a broader VUV photon range emitted by an H_2 plasma discharge lamp. We fit the new set of ion cross section data with a power law,

$$\sigma_d^{CR}[\mathrm{cm}^2] = \alpha S_e^{\beta}, \tag{3}$$

leading to the parameters

$$\log_{10}(\alpha) = -17.09 \pm 0.5;\ \beta = 1.57 \pm 0.21, \tag{4}$$

where σ_d^{CR} is the CH destruction cross section, α and β are fitting parameters, and S_e is the stopping power in eV/Å. By adding these three new measurements, the resulting slope is further constrained by high energies and slightly higher than determined previously. There is no pronounced temperature dependence of the destruction cross sections, as can be seen in Table 1. To extend and apply these measurements to astrophysical environments, we must sum the effect over the cosmic ray ion abundances and energy distribution contributions. The destruction rate R_d^{GCR} of the CH bonds in interstellar a-C:H by cosmic rays can be calculated by

$$R_d^{GCR}\left[s^{-1}\right] = 4\pi \sum_Z \int_{E_A^{min}}^{\infty} \sigma_d^{CR}(E_A, Z) \frac{dN}{dE_A}(E_A, Z) dE_A, \tag{5}$$

where $\sigma_d^{CR}[\mathrm{cm}^2]$ is the destruction cross section monitored by CH bonds, and $\frac{dN}{dE_A}(E_A, Z)$[particles cm^{-2} s^{-1} sr^{-1}/(MeV/u)] is the differential flux of the cosmic ray element of atomic number Z, with a cutoff in energy E_A^{min} set at 100 eV/u. Moving the cutoff from 10 eV/u to 1 keV/u does not change the results significantly. The differential flux for different Z follows the GCR observed relative abundances from Wang et al. (2002; H,He); de Nolfo et al. (2006; Li, Be); and George et al. (2009) (>Be), as explained in greater detail in Dartois et al. (2013). The integration is performed up to $Z = 28$ corresponding to Ni; a significant drop in the cosmic abundance and thus the contribution is observed above. The cross section $\sigma_d^{CR}(E_A, Z)$ is evaluated by combining the cross section dependence $\sigma_d^{CR}(S_e)$ established experimentally and the calculated electronic stopping power S_e using the SRIM code (Ziegler et al. 2010) as a function of atomic number Z and specific energy E_A (in MeV per nucleon). For the differential Galactic cosmic ray flux we adopt the functional form given by Webber & Yushak (1983) for primary cosmic ray

spectra using the leaky box model, also described in Shen et al. (2004)

$$\frac{dN}{dE_A}(E_A, Z) = \frac{C\ E_0^{0.3}}{(E_A + E_0)^3}, \quad (6)$$

where C is a normalization constant (=9.42 × 10^4, Shen et al. 2004). Under this parameterization, the differential flux dependence at high energy goes asymptotically to a −2.7 slope. Unless close to a strong emitting source (like a supernova), the propagation of cosmic rays in the diffuse ISM (GALPROP model, e.g., Jóhannesson et al. 2016), the Local ISM (e.g., Cummings et al. 2016; Bisschoff & Potgieter 2016) and in dense molecular clouds (e.g., Chabot 2016), flattens the distribution in the low-energy range. The E_0 form parameter allows the less known low-energy cosmic rays contribution to be adjusted, and thus influences the resulting ionization rate. Typical adopted conservative values for E_0 to explore different propagated distributions are taken between 200 and 600 MeV/u (e.g., Shen et al. 2004). The ionization rate (ζ) corresponding to the same distribution can also be calculated (Sect. 4.4.2 in Dartois et al. 2013), and gives an observable that can be compared with astrophysical observations obtained in various environments (e.g., McCall et al. 2003; Geballe & Oka 2010; Indriolo & McCall 2012).

The calculated destruction timescales ($\tau = 1/R_d^{GCR}$) associated with the destruction rates for E_0 = 150−600 MeV/u are shown in Fig. 10. (in the range of $R_d^{GCR} \approx 1.7 \times 10^{-15}$–$3.9 \times 10^{-17}$ s^{-1}), and the related calculated ionization rates are reported on the other axis (in the range $\zeta \approx 7 \times 10^{-16}$–$2 \times 10^{-17}$ s^{-1}).

Interstellar ionization rates observed for n_H column densities in range from 10^{21} to a few 10^{23} cm^{-2} fall in the range $1.7 \pm 1.3 \times 10^{-16}$ s^{-1} < ζ < $1.06 \pm 0.82 \times 10^{-15}$ s^{-1} (Fig. 19 in Indriolo & McCall 2012). In Fig.10 we report the position of the mean value associated with these observations corresponding to an ISM mean ionization rate of $\zeta = 3.5 \times 10^{-16}$ s^{-1}. We also report the value for the dense cloud measurements (N_H column density ≈ 10^{23}cm^{-2}), around $\zeta = 5 \times 10^{-17}$ s^{-1}.

The calculated destruction rates by cosmic rays corresponding to these ionization rates show that the a-C:H dust grains are relatively resilient against cosmic rays, with corresponding destruction timescales of ≈4 × 10^7 yr in the diffuse ISM, compared to about ≈10^4 yr with VUV photons (e.g., Alata et al. 2014; Godard et al. 2011; Mennella et al. 2001). The destruction timescale reaches above ≈3 × 10^8 yr in the shielded dense clouds, longer than the typical lifetime of the dense cloud phase where their impact increases as the DISM VUV photons are attenuated and only the cosmic ray induced VUV photons coexist.

4.2. Species formation

The corresponding formation rate of a species X (=H_2, CH_4, C_2H_2...) reads

$$R_f^{GCR}(X)[cm^{-3}s^{-1}] = \frac{n(CH)}{n_{tot}} n_{tot}[cm^{-3}]\, R_d^{GCR}[s^{-1}]\, \eta(X), \quad (7)$$

where $\frac{[n(CH)]}{[n_{tot}]} = f^C_{aCH} \times \frac{[C]}{[H]}$, with f^C_{aCH} being the fraction of interstellar carbon abundance locked into a-C:H; $n_{tot} = n(H) + 2n_{H_2}$ is the total number density of hydrogen atoms; and $\eta(X)$ is the production yield of a given species (see Tables 3–5, being ≈0.9−1. for H_2, one to two orders of magnitude lower for CH_4, C_2H_2 ...). The carbon cosmic abundance $\frac{[C]}{[H]}$ is debated. We adopt a typical value of 3 × 10^{-4} (e.g., Parvathi et al. 2012; Sofia et al. 2011; Sofia & Meyer 2001, and references therein). We assume that about 5 to 10% of the cosmic carbon is locked in a-C:H (i.e., $f^C_{a-C:H}$ = 0.05−0.1), which is a conservative value given that it is observed ubiquitously (e.g., Godard et al. 2012; Dartois & Muñoz-Caro 2007; Furton et al. 1999, and references therein). Then:

$$R_f^{GCR}(X)[cm^{-3}\ s^{-1}] = 1.5\text{–}3 \times 10^{-5} n_{tot}[cm^{-3}] R_d^{GCR}[s^{-1}]\, \eta(X). \quad (8)$$

At steady state, in the diffuse medium, the formation balances the destruction rate,

$$R_f^{GCR}(X)[cm^{-3}\ s^{-1}] \approx Rd_X(0)\, \chi\, e^{-\tau_d} f_s[N(X)]\, n_X, \quad (9)$$

where $Rd_X(0)$ is the unshielded photodissociation rate per species X for χ = 1, and $f_s[N(X)]$ is the X self-shielding factor at a given $N(H)[cm^{-2}]$ column density from the far-UV photon source. The molecular abundance for species X is therefore given by

$$\frac{n_X}{n_{tot}} = \frac{1.5\text{–}3 \times 10^{-5}\, R_d^{GCR}[s^{-1}]\, \eta(X)}{Rd_X(0)\, \chi\, e^{-\tau_d} f_s[N(X)]}. \quad (10)$$

The gas-phase released hydrocarbons will be efficiently photodissociated (photodissociation rate $CH_4 \approx 1.2 \times 10^{-9}$ s^{-1}, $C_2H_2 \approx 3.3 \times 10^{-9}$ s^{-1}, van Dishoeck et al. 2006).

By comparing the ionization rate mean value for the diffuse medium found by Indriolo & McCall 2012 ($\zeta = 3.5 \times 10^{-16}$ s^{-1}, the astrophysical observable anchor point) to the ionization rate derived from our calculation for various E_0, shown in Fig. 10, it corresponds to a destruction rate of $R_d^{GCR} \approx 8 \times 10^{-16}$ s^{-1} (destruction timescale $\tau \approx 4 \times 10^7$ yr). Adopting this value in the equation leads to

$$\frac{n_X}{n_{tot}} \approx \frac{1 - 2 \times 10^{-11} \eta(X)}{e^{-\tau_d} f_s[N(X)]}. \quad (11)$$

In the diffuse interstellar medium the observed fractional abundance of small hydrocarbons from CH_y to C_4H_y lies in the 10^{-8}–10^{-9} range (e.g., Liszt et al. 2012; Liszt & Gerin 2016). Even if cosmic ray irradiation of a-C:H contributes to replenishing the hydrocarbons reservoir, putting the numbers ($\tau_d \ll 1, f_s[N(X)] \approx 1, \eta(X) \leq 10^{-2}$) in Eq. (11), it is not sufficient to explain such abundances.

Cosmic ray (CR) irradiations take an increasing importance in intermediate to dense regions where the high-energy CR component penetrates deep and thus R_d^{GCR} decreases slowly (as observed using the H_3^+ tracer for ζ by Indriolo & McCall 2012, Fig. 19 up to column densities exceeding 10^{23} H cm^{-2}), whereas the photodissociation term $e^{-\tau_d}$ rapidly goes to zero (10^{-3} at $A_V \approx 7$) and the fractional abundance from Eq. (10) thus increases to values compatible with observations and models (Guzmán et al. 2015; Alata et al. 2015; Pety et al. 2012).

5. Conclusion

Thin hydrogenated amorphous carbon films, astrophysical analogues giving rise to the widespread absorption observed at 3.4 μm in the diffuse medium of galaxies, were irradiated with high-energy Au, Xe, and C ions at the GSI UNILAC accelerator, at room temperature and at low temperature. The radiolytic destruction was followed by infrared spectroscopy of the solid phase and the chemical species produced and released upon irradiation were measured quantitatively by mass spectrometry.

The main radiolysis product is H_2, participating in the dehydrogenation of the a-C:H in an astrophysical context. These irradiations show that the production of numerous small hydrocarbons (C_xH_y; $x = \{1, 4\}$) is efficient with swift heavy ions, and increases over the H_2 production with the deposited energy.

The cross sections derived for the interaction with swift heavy ions were implemented in an astrophysical model showing that the effect of CR irradiations are important in intermediate to dense regions where the high-energy CR component penetrates much deeper with respect to the external UV field and reaches at depth an equilibrium with the secondary UV field produced by cosmic ray interaction with H_2.

The production of these carbonaceous species will contribute to eroding the a-C:H dust grains. The extent of this process will depend on the hydrogen content of the interstellar dust grains. If the hydrogen content is high, either intrinsically or via hydrogenation by interaction with the ambient hydrogen gas, the production of small volatile carbonaceous species is efficient, and leads to the complete destruction of the grains while the species released enrich the gas phase chemistry. We expect that this efficiency will decrease if the hydrogen content gets much lower and that the grains will eventually convert into a polyaromatic structure. The species released during experiments simulating the cosmic ray ions, starting with less hydrogenated, more polyaromatic interstellar analogues, will be further investigated using dedicated forthcoming experiments.

Acknowledgements. The authors would like to cordially thank the anonymous referee for the comments that improved the scientific content of the article, as well as H. Kinnan for suggestions on the language and structure of the manuscript. The experiments were performed at the (GSI) Darmstadt, Germany. Part of this work was supported by the French INSU-CNRS program "Physique et Chimie du Milieu Interstellaire" (PCMI).

References

Alata, I., Cruz-Diaz, G. A., Muñoz Caro, G. M., & Dartois, E. 2014, A&A, 569, A119
Alata, I., Jallat, A., Gavilan, L., et al. 2015, A&A, 584, A123
Bisschoff, D., & Potgieter, M. S. 2016, Ap&SS, 361, 48
Boogert, A. C. A., Schutte, W. A., Helmich, F. P., Tielens, A. G. G. M., & Wooden, D. H. 1997, A&A, 317, 929
Boudin, N., Schutte, W. A., & Greenberg, J. M. 1998, A&A, 331, 749
Chabot, M. 2016, A&A, 585, A15
Cummings, A. C., Stone, E. C., Heikkila, B. C., et al. 2016, ApJ, 831, 18
Dartois, E., & Muñoz-Caro, G. M. 2007, A&A, 476, 1235
Dartois, E., Marco, O., Muñoz-Caro, G. M., et al. 2004, A&A, 423, 549
Dartois, E., Ding, J. J., de Barros, A. L. F., et al. 2013, A&A, 557, A97
Fuente, A., Rodrıguez-Franco, A., Garcıa-Burillo, S., Martın-Pintado, J., & Black, J. H. 2003, A&A, 406, 899
Furton, D. G., Laiho, J. W., & Witt, A. N. 1999, ApJ, 526, 752
Gavilan, L., Alata, I., Le, K. C., et al. 2016, A&A, 586, A106
Gerin, M., Roueff, E., Le Bourlot, J., et al. 2005, Astrochemistry: Recent Successes and Current Challenges, 231, 153
Geballe, T. R., & Oka, T. 2010, ApJ, 709, L70
George, J. S., Lave, K. A., Wiedenbeck, M. E., et al. 2009, ApJ, 698, 1666
Gerakines, P. A., & Hudson, R. L. 2015, ApJ, 805, L20
Godard, M., & Dartois, E. 2010, A&A, 519, A39
Godard, M., Féraud, G., Chabot, M., et al. 2011, A&A, 529, A146
Godard, M., Geballe, T. R., Dartois, E., & Muñoz Caro, G. M. 2012, A&A, 537, A27
Guzmán, V. V., Pety, J., Goicoechea, J. R., et al. 2015, ApJ, 800, L33
Herrero, V. J., Gálvez, Ó., Maté, B., & Escribano, R. 2010, Phys. Chem. Chem. Phys. (Incorporating Faraday Transactions), 12, 3164
Hudson, R. L., Ferrante, R. F., & Moore, M. H. 2014, Icarus, 228, 276
Indriolo, N., & McCall, B. J. 2012, ApJ, 745, 91
Jóhannesson, G., Ruiz de Austri, R., Vincent, A. C., et al. 2016, ApJ, 824, 16
Kerkhof, O., Schutte, W. A., & Ehrenfreund, P. 1999, A&A, 346, 990
Khanna, R. K., Ospina, M. J., & Zhao, G. 1988, Icarus, 73, 527
King, S. J., & Price, S. D. 2007, J. Chem. Phys., 127, 174307
Knez, C., Moore, M. H., Ferrante, R. F., & Hudson, R. L. 2012, ApJ, 748, 95
Liszt, H. S., & Gerin, M. 2016, A&A, 585, A80
Liszt, H., Sonnentrucker, P., Cordiner, M., & Gerin, M. 2012, ApJ, 753, L28
McCall, B. J., Huneycutt, A. J., Saykally, R. J., et al. 2003, Nature, 422, 500
Mennella, V., Muñoz Caro, G. M., Ruiterkamp, R., et al. 2001, A&A, 367, 355
Mennella, V., Baratta, G. A., Esposito, A., Ferini, G., & Pendleton, Y. J. 2003, ApJ, 587, 727
de Nolfo, G. A., Moskalenko, I. V., Binns, W. R., et al. 2006, Adv. Space Res., 38, 1558
Parvathi, V. S., Sofia, U. J., Murthy, J., & Babu, B. R. S. 2012, ApJ, 760, 36
Pety, J., Gratier, P., Guzmán, V., et al. 2012, A&A, 548, A68
Pilleri, P., Joblin, C., Boulanger, F., & Onaka, T. 2015, A&A, 577, A16
Roth, A. 1990, Vacuum Technology (Amsterdam: North-Holland Publ.)
Sandford, S. A., & Allamandola, L. J. 1993, ApJ, 409, L65
Shen, C. J., Greenberg, J. M., Schutte, W. A., & van Dishoeck, E. F. 2004, A&A, 415, 203
Sofia, U. J., & Meyer, D. M. 2001, ApJ, 554, L221
Sofia, U. J., Parvathi, V. S., Babu, B. R. S., & Murthy, J. 2011, AJ, 141, 22
Straub, H. C., Renault, P., Lindsay, B. G., Smith, K. A., & Stebbings, R. F. 1996a, Phys. Rev. A, 54, 2146
Straub, H. C., Lindsay, B. G., Smith, K. A., & Stebbings, R. F. 1996b, J. Chem. Phys., 105, 4015
Straub, H. C., Lin, D., Lindsay, B. G., Smith, K. A., & Stebbings, R. F. 1997, J. Chem. Phys., 106, 4430
Straub, H. C., Lindsay, B. G., Smith, K. A., & Stebbings, R. F. 1998, J. Chem. Phys., 108, 109
Teyssier, D., Fossé, D., Gerin, M., et al. 2004, A&A, 417, 135
Van Dishoeck, E. F., Jonkheid, B., & van Hemert, M. C. 2006, Faraday Discussions, 133, 231
Wang, J. Z., Seo, E. S., Anraku, K., et al. 2002, ApJ, 564, 244
Ward, M.D., King, S. J. , & Price, S. D. 1998, J. Chem. Phys. 134, 024308
Webber, W. R., & Yushak, S. M. 1983, ApJ, 275, 391
Wohrer, K., Chabot, M., Fossé, R., & Gardès, D. 2000, Rev. Sci. Instr., 71, 2025
Ziegler, J. F., Ziegler, M. D., & Biersack, J. P. 2010, Nuclear Instruments and Methods in Physics Research B, 268, 1818